5-2015

Phase field modeling and simulation of dendritic growth with varying latent heat and seeding distributions

Jordan W. Key
University of Arkansas, Fayetteville

Phase field modeling and simulation of dendritic growth with varying latent heat and seeding distributions

An Undergraduate Honors College Thesis

in the

Department of Mechanical Engineering
College of Engineering
University of Arkansas
Fayetteville, AR

by

Jordan Walker Key

This thesis is approved.

Thesis Advisor:

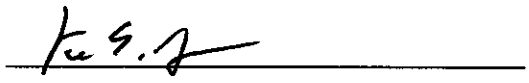

Thesis Committee:

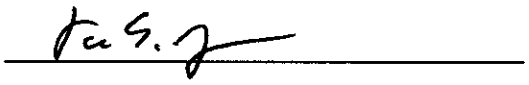

Acknowledgements

Sincere thanks and deepest gratitude are due to Dr. Doug Spearot for his mentorship, patience, and advice over the course of this research and writing. This work would not have been possible without his constant efforts to see it become a success. Thanks are also due to Drs. John and Gay Stewart for their efforts to ensure this work was of proper quality.

Table of Contents

1. INTRODUCTION

The process of solidification is generally considered to be one of the most important materials manufacturing methods, and has fundamental implications during the casting of metals. In addition, solidification is the critical step in the manufacturing of many other materials such as thermoplastic polymers, ceramics, and inorganic glasses [1]. Any solid product that is molten at any point during its processing necessitates solidification, even if there are additional processing steps that occur. For example, large slabs of metal are often produced from a melt and are worked and shaped in a secondary process to achieve the desired final form. Although the most significant processing occurs when the slab is solid, the previous solidification still plays a role in the properties of the material. Solidification is also used as a primary processing step, such as in casting of aluminum wheels for automobiles. According to the International Organization of Motor Vehicle Manufacturers (OICA), the United States produced 11,066,432 motor vehicles in 2013 [2]. Considering that motor vehicles typically have at least four wheels, one can appreciate the importance of casting to the automotive industry. Soldering and brazing techniques, used to repair leaks in copper tubing, also utilize solidification as the underlying principle.

It is important to keep in mind that solidification can be controlled; by carefully adjusting the factors involved, such as time and temperature, the desired material properties can be achieved. Various different results are obtained when using forced cooling versus free cooling or with undercooling versus without undercooling. Indeed, this is the essence of materials science and engineering: the ability to study materials,

their properties, and the processes used to produce them in order to manipulate and control those properties to meet our designs.

The phase field modeling method is a powerful tool used to simulate microstructural evolution in a system at the mesoscale (the scale that lies between the nanoscale and the macroscale). Among the vast number of applications of the phase field method are simulations of solidification, martensitic transformation and grain growth, precipitate growth and coarsening, and various solid-state transformations including crack propagation [3]. The phase field method describes microstructure evolution by employing a set of phase field variables that represent both conserved and non-conserved quantities, depending on the application [4]. Examples of conserved variables include concentration and molar fraction [3]. Non-conserved variables are much more common and typically include order parameters and phase variables. Phase variables constitute the core of the model. A continuous field is made up of these non-conserved phase variables over the entire spatial domain of the system. Specifically, in the case of solidification, a single phase variable p may be employed. The case where $p = 0$ represents liquid and the case where $p = 1$ represents a solid. The interface is formed by the continuous variation of p over a narrow region between the bulk liquid ($p = 0$) and the bulk solid ($p = 1$). A temperature field would also follow a specified evolution, varying continuously across the simulation domain. This is known as the diffuse-interface description, as opposed to the sharp-interface description in which the interface is a singular dividing surface. [5].

The great advantage in using the diffuse-interface description lies in the fact that the interface is not explicitly tracked at every time step in the simulation; rather, the interface is implicitly described by the continuous set of phase field variables. This makes

computation much less complex and allows for more complicated evolutions to be simulated. Furthermore, no boundary conditions need to be specified at the moving interface and *a priori* assumptions about the conditions at the interface are not required [3].

The mechanism that drives the microstructure evolution is the reduction of the system's free energy, which is primarily composed of a bulk energy and an interfacial energy. The free energy function, in the case of solidification simulations, typically takes the form of a double-well potential with the stationary states corresponding to the equilibrium values of the phase variables [6]. Gradient energy coefficients cause energy penalties where interfaces are present, and these penalties balance with the tendency for the system to achieve a single bulk phase to produce a finite, diffuse interface [7]. Differentiation of the free energy functional yields evolution equations for the system through time. The result is a set of coupled partial differential equations.

The phase field method was initially developed to describe the solidification of pure materials, but has since been extended to the solidification of alloys and a vast number of other problems [8]. Kobayashi presented both an isotropic and anisotropic model of solidification and crystal growth in pure materials, particularly for the modeling of dendrites and snowflakes [6]. At a later time, Warren, Kobayashi, Lobkovsky, and Carter were able to extend the phase field model to the solidification of pure polycrystalline systems [8]. Others were also able to apply phase fields to polycrystalline systems [9,10].

The first phase of this work will be to present and compare such models, as well as develop a MATLAB code that can reproduce the prior results of Kobayashi et al.

Then, the objective of this work is to employ the Kobayashi isotropic and anisotropic models and the MATLAB code to study various solidification and growth behaviors of systems with different latent heats. Different initial seedings will be explored and the latent heat parameter will be manipulated to determine its effect on the solidification of the system in question.

2. KOBAYASHI MODEL

Kobayashi sought to present a simple model that could sufficiently describe the dendritic growth seen in solidification applications and naturally in snowflakes. In his model, the process limiting the crystal growth was the latent heat, represented by the value *K* [6]. The phase variables of the model were the phase, *p*, and the temperature, *T*. The following Ginzburg-Landau type free energy was adopted [6]:

$$\Phi[p;m] = \int \frac{1}{2}\varepsilon^2 |\nabla p|^2 + F(p;m)\, dr\,. \tag{1}$$

In this formulation, ε is a small constant that determines the interface thickness. It is a microscopic interaction length and controls the mobility of the interface [6]. As explained above, *F* is a double-well potential that has local minima at $p = 0$ and $p = 1$. Specifically, *F* has the following form [6]:

$$F(p;m) = \frac{1}{4}p^4 - \left(\frac{1}{2} - \frac{1}{3}m\right)p^3 + \left(\frac{1}{4} - \frac{1}{2}m\right)p^2\,. \tag{2}$$

In the above equation, $|m| < 0.5$. The parameter *m* determines the tilt of the double well, and the difference between the minima is proportional to *m*. That is, when $m = 0$ the

minima have equal *F*-values. When *m* is negative, the *F*-value of the solid well is greater and vice versa. Anisotropy will be discussed later in this paper; for now, discussion is limited to the isotropic model.

As stated above, differentiation of the free energy yields the time evolution equations. In the two-dimensional case, we have [6]:

$$\tau \frac{\partial p}{\partial t} = -\frac{\partial}{\partial x}\left(\varepsilon \varepsilon' \frac{\partial p}{\partial y}\right) + \frac{\partial}{\partial y}\left(\varepsilon \varepsilon' \frac{\partial p}{\partial x}\right) + \nabla \cdot (\varepsilon^2 \nabla p) + p\,(1-p)\,(p - \frac{1}{2} + m)\,. \quad (3)$$

Under the isotropic assumption, ε'= dε/dθ becomes zero and the result is simply the latter half of the equation:

$$\tau \frac{\partial p}{\partial t} = \varepsilon^2 \nabla^2 p + p\,(1-p)\,(p - \frac{1}{2} + m)\,. \quad (4)$$

For simplicity, one can define a function $g(p)$ such that $g(p) = p\,(1\text{-}p)\,(\text{p-}0.5\text{+}m)$. From classical thermodynamics, the time evolution of the temperature field is given by [6]:

$$\frac{\partial T}{\partial t} = \nabla^2 T + K \frac{\partial p}{\partial t}\,. \quad (5)$$

K is proportional to the latent heat, as stated before. With Eqs. (4) and (5), the two most crucial parts of the model, the field evolution equations, are known.

To solve these equations, an explicit finite difference approach is used. The convention of a forward-time, center-space approximation is desirable for its simplicity. The spatial and time derivatives are defined as [11,12]:

$$\frac{\partial p}{\partial t} = \frac{p_{new} - p}{\Delta t} + O(h) \quad (6)$$

$$\frac{\partial^2 p_{j,i}}{\partial x^2} = \frac{p_{j,i+1} - 2p_{j,i} + p_{j,i-1}}{(\Delta x)^2} + O(h^2). \quad (7)$$

The forward difference approximation (Eq. (6)) is first-order accurate and the center difference approximation (Eq. (7)) is second-order accurate. The above equations use the general presentation, *h*, for the discretized step size in the error. In this case, it would be Δt in time and either Δx or Δy in space. In two dimensions, the finite difference approach leads to a five-point stencil, in which the value of the phase variables at one point are determined by the values of those variables at four neighboring points (two in each direction). This correctly ensures that evolution only occurs appropriately close to the boundary, and is a physically sufficient approximation. With the finite difference approach, the evolution equations become:

$$\tau\left(\frac{p_{new} - p}{\Delta t}\right) = \varepsilon^2\left(\frac{(p_{j,i+1} - 2p_{j,i} + p_{j,i-1})}{(\Delta x)^2} + \frac{(p_{j+1,i} - 2p_{j,i} + p_{j-1,i})}{(\Delta y)^2}\right) + g(p) \quad (8)$$

$$\frac{T_{new} - T}{\Delta t} = \left(\frac{(T_{j,i+1} - 2T_{j,i} + T_{j,i-1})}{(\Delta x)^2} + \frac{(T_{j+1,i} - 2T_{j,i} + T_{j-1,i})}{(\Delta y)^2}\right) + K\left(\frac{p_{new} - p}{\Delta t}\right). \quad (9)$$

The phase equation is solved first by the finite difference approximations, then the temperature field is solved in the same manner. After algebraic manipulation:

$$p_{new} = p + \frac{\varepsilon^2 \Delta t}{\tau}\left(\frac{(p_{j,i+1} - 2p_{j,i} + p_{j,i-1})}{(\Delta x)^2} + \frac{(p_{j+1,i} - 2p_{j,i} + p_{j-1,i})}{(\Delta y)^2}\right) + \frac{g(p)\Delta t}{\tau} \quad (10)$$

$$T_{new} = T + \Delta t\left(\frac{(T_{j,i+1} - 2T_{j,i} + T_{j,i-1})}{(\Delta x)^2} + \frac{(T_{j+1,i} - 2T_{j,i} + T_{j-1,i})}{(\Delta y)^2}\right) + K(p_{new} - p). \quad (11)$$

Equations (10) and (11) are simple, algebraic equations to solve for the field variables at each time step. These equations are programmed into MATLAB. First, a system domain is defined. In this case, the domain was a 12x3 array divided into squares of side length 0.03. This yielded 400 pixels in the horizontal direction and 100 in the vertical direction. Next, a set of initial conditions is determined.

In this problem, the system is initially entirely undercooled ($T = 0$). Most of the system is liquid ($p = 0$), except for a wall ten pixels across which is solid ($p = 1$). This initial left wall of the system is the seed from which the solidification will proceed. The initial conditions of the system are shown in the two figures below.

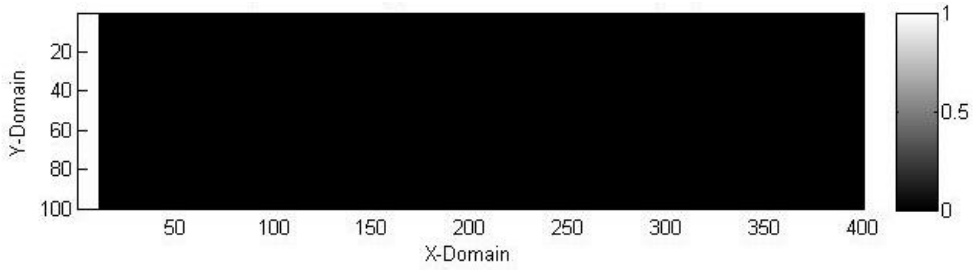

Fig. 1. Initial conditions of the phase field. White is solid, black is liquid.

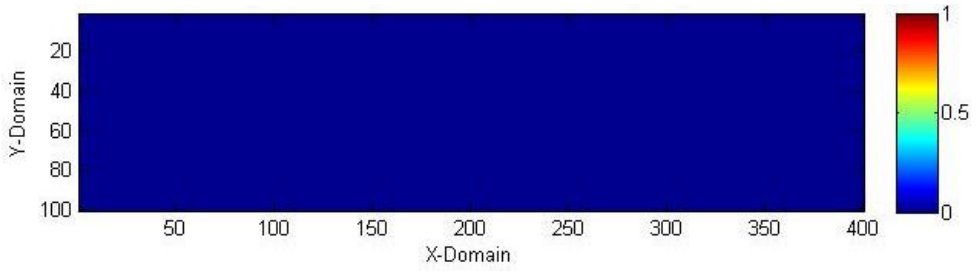

Fig. 2. Initial conditions of the temperature field. Blue is the undercooled temperature, red is the equilibrium.

Now that the initial conditions of the system have been established, the evolution of the field variables may begin. A time loop is created, and over each time step both *m* and *g* are calculated as follows [6]:

$$m = \frac{\alpha}{\pi} * \text{atan}(\gamma[1 - T]) \tag{12}$$

$$g = p.*(1-p).*(p-0.5+m) + a*p.*(1-p).*(0.5-rand[size(p)]). \tag{13}$$

The second half of the equation for *g* is a term to add random thermal noise to the system [6]. The above fixed parameters must are defined as: $\alpha = 0.9$, $\varepsilon = 0.01$, $\tau = 0.003$, $\Delta t = 0.0002$, $a = 0.01$, and $\gamma = 10$. Alpha is a positive constant used in calculating *m*, and must remain less than one in order to satisfy the earlier relation that $|m| < 0.5$. Epsilon, as discussed previously, determines the thickness of the interface. Tau is a time constant, and Δt is the time mesh size or time step. Gamma is another constant required to determine *m*, and *a* is a constant used to introduce random thermal noise into the system. Before evolving the system at each step, *m* and *g* are calculated using the values at the previous step (or in the first case initial conditions). Next in the time loop, after *m* and *g* are evaluated, every point in the array is evolved according to Equations (10) and (11). First, however, certain boundary conditions must be imposed. Thermal energy is to be transferred solely through the interface; therefore, a no-flux condition is imposed on the boundaries of the system. This requires that all values adjacent to but outside of the border of the system be equal to all values adjacent to and inside the border. Whenever a term in the finite difference approximation would call for a value that is outside of the domain of the system, it is substituted with the adjacent value inside the system. For example, at the top wall of the box,

$$p(j,i-1) \rightarrow p(j,i+1), \tag{14}$$

because at the top of the box $i = 1$ and there is no i-1 value. Due to the no-flux condition, the i-1 term has the same value as the i+1 term. This means that the problem of calling for a non-existent value in MATLAB is solved.

Now that the boundary conditions have been established, actual evolution can take place. Each point is evaluated to see if it is on a boundary or if it is an interior point. Appropriate substitutions are made (or not) and then both the phase (Eq. (10)) and temperature equation (Eq. (11)) are solved for the point. Each new value is saved and becomes and old value for the purposes of calculating the next step.

The change of growth behavior under different latent heats is of interest. Generally, as K increases the growth rate decreases and the front becomes less stable and develops dendritic branching. The slowing of the growth rate is due to the latent heating process out-pacing the thermal energy removal process, causing the local temperature to rise and growth to slow until the thermal energy removal process can match the heating process [13]. Figures 3-5 below are for isotropic growth with value $K = 0.8$ at $t = 0.1$ s, $t = 0.3$ s, and $t = 0.5$ s, respectively. This is shown in the figures as steps 500, 1500, and 2500 (keeping in mind the time step is 0.0002 s).

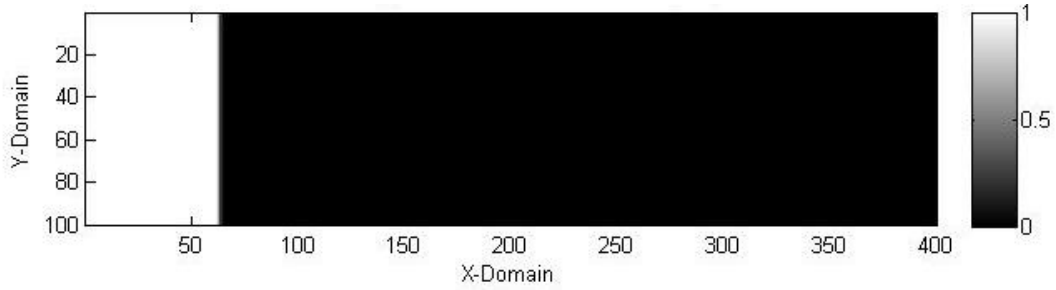

Fig. 3. Phase variable during isotropic microstructure evolution when K = 0.8, step 500.

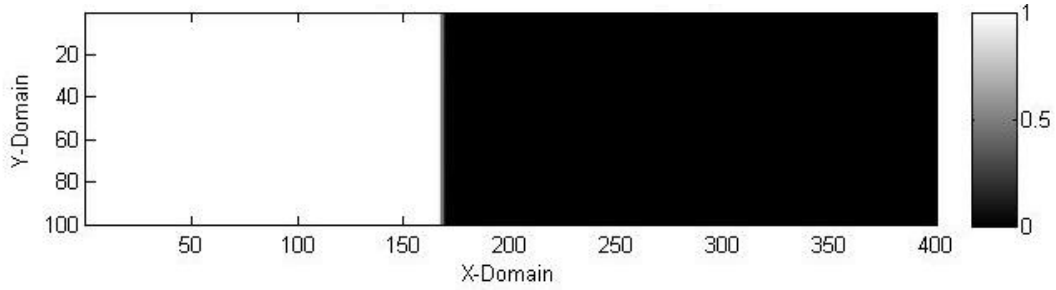

Fig. 4. Phase variable during isotropic microstructure evolution when K = 0.8, step 1500.

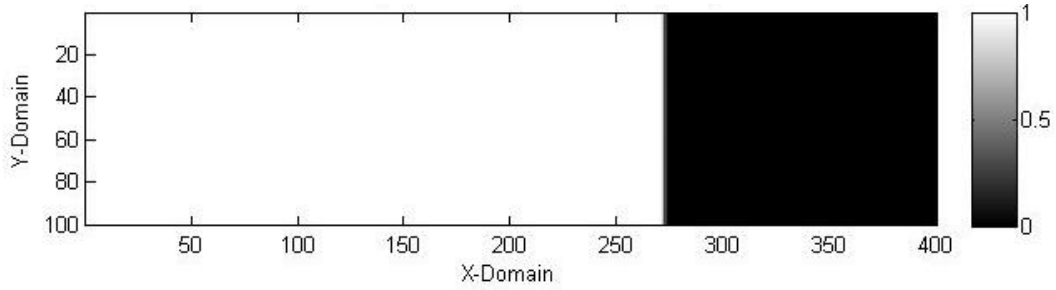

Fig. 5. Phase variable during isotropic microstructure evolution when K = 0.8, step 2500.

Clearly the growth front advances in a very stable fashion, maintaining an extremely flat vertical wall. Nearly three-quarters of the domain solidifies as the front reaches halfway between the 250-pixel and 300-pixel mark. Figures 6-8 below show the same amount of time elapsing in the case of K = 1.0.

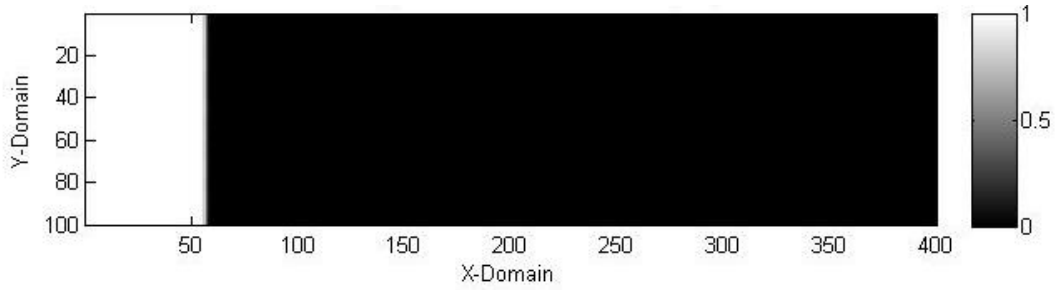

Fig. 6. Phase variable during isotropic microstructure evolution when K = 1.0, step 500.

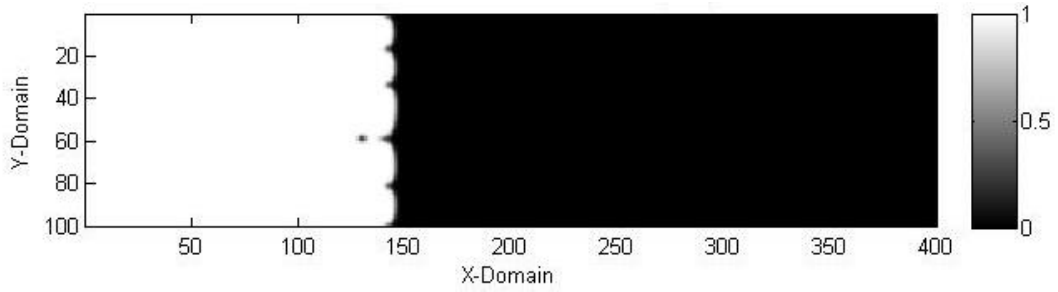

Fig. 7. Phase variable during isotropic microstructure evolution when K = 1.0, step 1500.

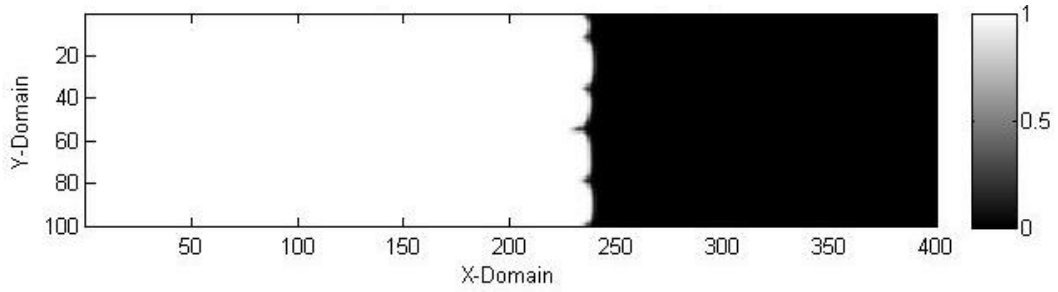

Fig. 8. Phase variable during isotropic microstructure evolution when K = 1.0, step 2500.

As the growth front advances, columnar roughness begins to form. If K is increased slightly more, this roughness will transition into holes (porosity) due to surface tension as the front advances [6]. One can also see that slightly over half of the domain has solidified by step 2500 when K = 1.0. Comparing this growth behavior to that when K = 1.6, shown below in Figures 9-11, one can see that the growth is much slower for the K = 1.6 case with strong columnar growth with branching.

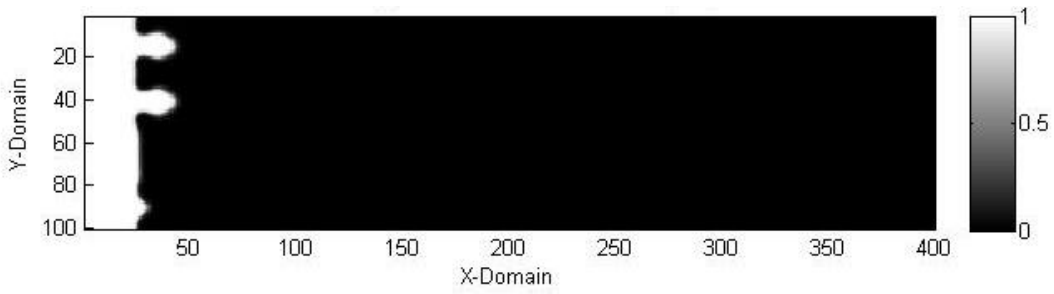

Fig. 9. Phase variable during isotropic microstructure evolution when K = 1.6, step 500.

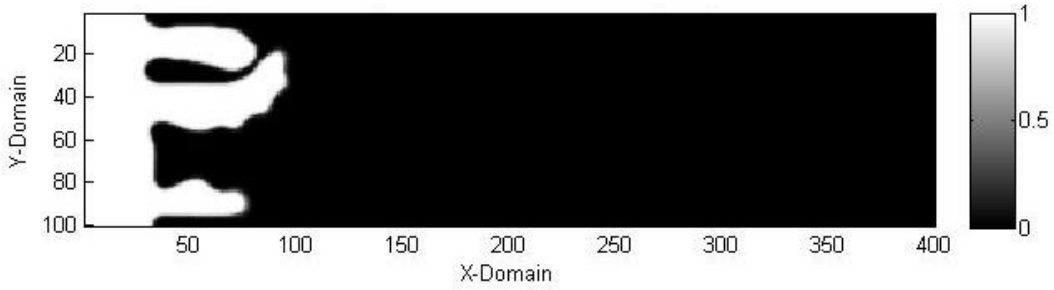

Fig. 10. Phase variable during isotropic microstructure evolution when K = 1.6, step 1500.

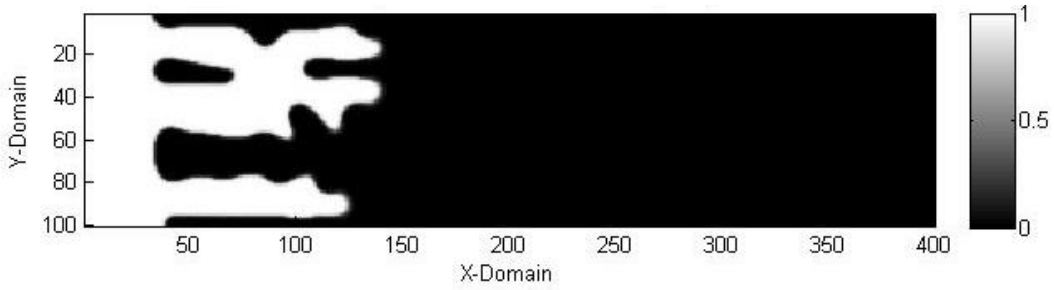

Fig. 11. Phase variable during isotropic microstructure evolution when K = 1.6, step 2500.

After 2500 steps, only a little over a quarter of the domain is solidified. The solidification wall that advances as a growth front in the previous case now stays mostly constant, while dendrites grow out of it and advance through the domain. Figures 12-14 show the temperature field for the K = 1.6 case at the three time steps. The latent heating and

thermal energy removal processes described above hold in every case in this work, so temperature fields will be produced here simply to show a typical temperature field evolution and will not be reproduced.

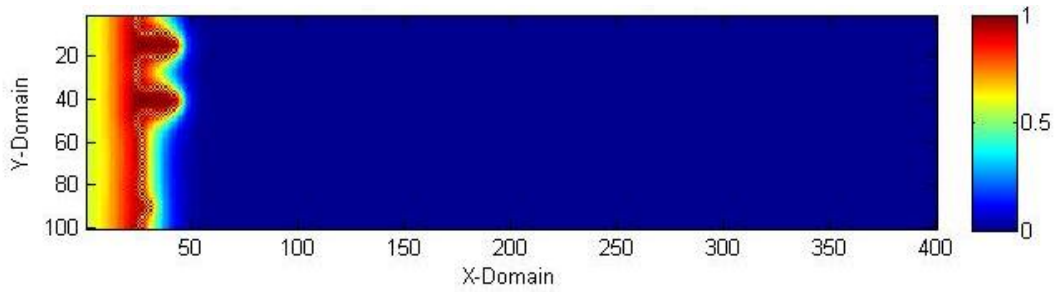

Fig. 12. Temperature variable during isotropic microstructure evolution when *K* = 1.6, step 500.

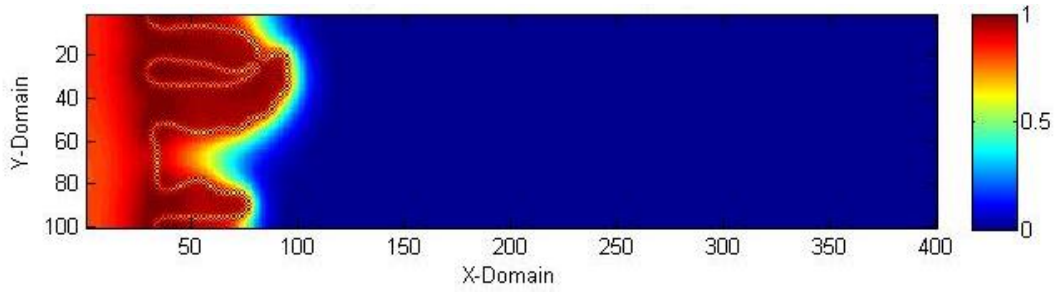

Fig. 13. Temperature variable during isotropic microstructure evolution when *K* = 1.6, step 1500.

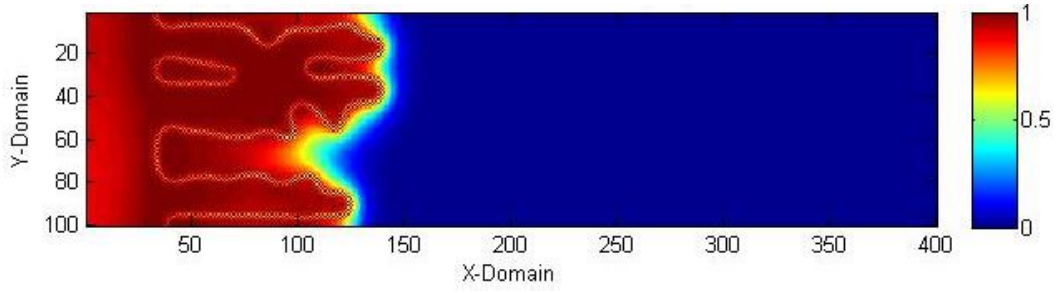

Fig. 14. Temperature variable during isotropic microstructure evolution when *K* = 1.6, step 2500.

Each of the results above are consistent with that of Kobayashi [6], validating the implementation of the phase field equations via the MATLAB code.

3. ANISOTROPIC MODEL

As stated previously, ε is a small parameter that determines the thickness of the interface. For the isotropic assumption to be dropped and anisotropy to be added to the model, ε is now assumed to depend on the direction of the outer normal vector to the interface (-∇p), following the work of Kobayashi [6]. This changes the Ginzburg-Landau type free energy to:

$$\Phi[p;m]=\int \frac{1}{2}\varepsilon(-\nabla p)^2\left|\nabla p\right|^2 + F(p;m)\,dr\,. \tag{15}$$

The outer normal vector to the interface is represented by -∇p and one can see that this is the only change made to the energy functional (Eq. (1)). Now ε is considered a function of the angle θ between the outer normal vector and the x-direction, which means ε' has a non-zero value (ε'=dε/dθ). As stated above, the time evolution of the phase field without isotropic assumptions is:

$$\tau\frac{\partial p}{\partial t} = -\frac{\partial}{\partial x}\left(\varepsilon\varepsilon'\frac{\partial p}{\partial y}\right)+\frac{\partial}{\partial y}\left(\varepsilon\varepsilon'\frac{\partial p}{\partial x}\right)+\nabla\cdot(\varepsilon^2\nabla p)+g(p)\,. \tag{16}$$

The right side of the equation consists of three primary parts (the function $g(p)$ is the same as before). These parts and their expansion are shown below.

$$-\frac{\partial}{\partial x}(\varepsilon\varepsilon'\frac{\partial p}{\partial y}) = -\varepsilon\frac{\partial\varepsilon'}{\partial x}\frac{\partial p}{\partial y}-\varepsilon'\frac{\partial\varepsilon}{\partial x}\frac{\partial p}{\partial y}-\varepsilon\varepsilon'\frac{\partial^2 p}{\partial y\partial x} \tag{17}$$

$$\frac{\partial}{\partial y}=\left(\varepsilon\varepsilon'\frac{\partial p}{\partial x}\right)=\varepsilon\frac{\partial\varepsilon'}{\partial y}\frac{\partial p}{\partial x}+\varepsilon'\frac{\partial\varepsilon}{\partial y}\frac{\partial p}{\partial x}+\varepsilon\varepsilon'\frac{\partial^2 p}{\partial x\partial y} \tag{18}$$

$$\nabla \cdot \left(\varepsilon^2 \nabla p\right) = \varepsilon^2 \frac{\partial^2 p}{\partial x^2} + \frac{\partial\left(\varepsilon^2\right)}{\partial x}\frac{\partial p}{\partial x} + \varepsilon^2 \frac{\partial^2 p}{\partial y^2} + \frac{\partial\left(\varepsilon^2\right)}{\partial y}\frac{\partial p}{\partial y} \tag{19}$$

In the anisotropic case, ε can be written in terms of a mean value and anisotropy function [6]:

$$\varepsilon = \bar{\varepsilon}\,\sigma(\theta) \tag{20}$$

$$\sigma(\theta) = 1 + \delta \cos\left[j\left(\theta - \theta_0\right)\right]. \tag{21}$$

Epsilon with the bar is a mean value of ε, whereas δ is the strength of the anisotropy and *j* is its mode number. This allows us to expand some of the variables in the above equations. It follows that:

$$\varepsilon = \bar{\varepsilon} + \bar{\varepsilon}\,\delta \cos\left[j\left(\theta - \theta_0\right)\right] \tag{22}$$

$$\varepsilon' = -\bar{\varepsilon}\,\delta\, j \sin\left[j\left(\theta - \theta_0\right)\right] \tag{23}$$

$$\varepsilon^2 = \bar{\varepsilon}^2 + 2\,\bar{\varepsilon}^2\,\delta \cos\left[j\left(\theta - \theta_0\right)\right] + \bar{\varepsilon}^2\,\delta^2 \cos^2\left[j\left(\theta - \theta_0\right)\right]. \tag{24}$$

In order to calculate the ε and ε' terms, θ must be defined and calculated at each point in the domain. According to Wheeler, the *x* and *y* partial derivatives of the phase have the relation $\tan\theta = p_y / p_x$ [14]. Therefore, the angle θ and its partial derivatives can be found as follows:

$$\theta = \operatorname{acos}\left(\frac{p_y}{\sqrt{p_y^2 + p_x^2}}\right) \tag{25}$$

$$\theta_x = \frac{p_x p_{xy} - p_y p_{xx}}{|\nabla p|^2} \tag{26}$$

$$\theta_y = \frac{p_x p_{yy} - p_y p_{xy}}{|\nabla p|^2}. \tag{27}$$

In the above, the subscript representation of the partial derivatives has been used for neatness. The inverse tangent function was originally used to calculate theta, but MATLAB did not properly calculate or evolve theta when this form was used. Implementing the equivalent relation using the inverse cosine function immediately rectified the situation. In order to avoid dividing by zero, a check for $|\nabla p|^2$ was implemented that would cause θ to become zero if $|\nabla p|^2$ was sufficiently small.

Finally, the evolution equation for the temperature field is the same as before. It is given again below:

$$\frac{\partial T}{\partial t} = \nabla^2 T + K\frac{\partial p}{\partial t}. \tag{28}$$

The above anisotropic model was programmed into the MATLAB code. As before, the initial domain was created and the fixed parameters were defined. The parameters are specified as follows: $\alpha = 0.9$, $\bar{\varepsilon} = 0.01$, $\tau = 0.0003$, $\gamma = 10$, $a = 0.01$, $\delta = 0.050$, $j = 4$, $\theta_0 = 0$, and K varies depending on the case in question. The time step is the same as before, the initial seed to initiate solidification is the same, and the calculation of m and g in the time loop is the same. However, the "if" statements that identify the location of the point with respect to the boundaries and ensure the no-flux condition are different for the anisotropic case. Whereas in the isotropic case only the second derivative

approximations of the phase and temperature were required, now in addition the first derivative approximations of the phase and temperature, as well as the cross derivative, are needed. Again following the forward-time, center-space convention, the spatial derivatives are used [11,12]:

$$\frac{\partial p_{j,i}}{\partial x} = \frac{p_{j,i+1} - p_{j,i-1}}{2\Delta x} + O(h^2) \tag{29}$$

$$\frac{\partial^2 p_{j,i}}{\partial x \partial y} = \frac{p_{j+1,i+1} - p_{j-1,i+1} - p_{j+1,i-1} + p_{j-1,i-1}}{4\Delta x \Delta y} + O(h^2). \tag{30}$$

Again, each point is evaluated to determine if it is an interior point or boundary and the appropriate substitution is made. The evolution equations are solved, the information is stored, and the figures are outputted in the same manner as before.

Similarly to the isotropic case, the evolution is more rapid and more stable for lower values of *K*. The figures below show anisotropic growth for when $K = 0.8$ at time steps 0, 500, 1500, and 2500. This corresponds with times $t = 0.1$ s, $t = 0.3$ s, and $t = 0.5$ s, just as before.

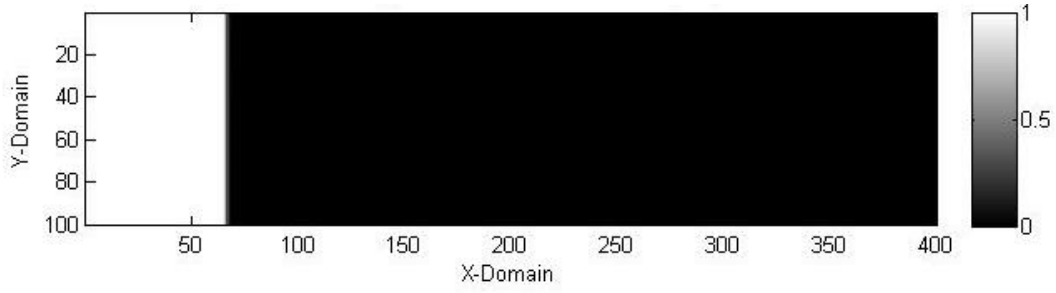

Fig. 15. Phase variable during anisotropic microstructure evolution when *K* = 0.8, step 500.

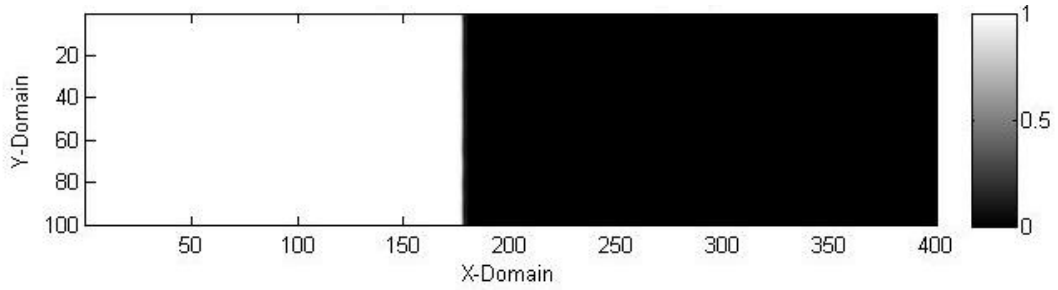

Fig. 16. Phase variable during anisotropic microstructure evolution when K = 0.8, step 1500.

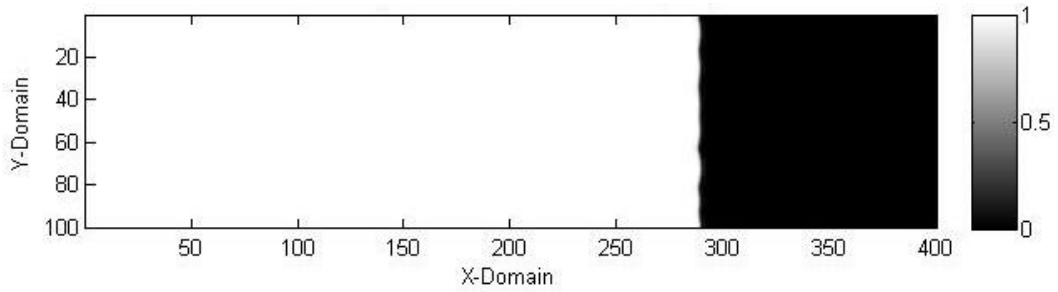

Fig. 17. Phase variable during anisotropic microstructure evolution when K = 0.8, step 2500.

Very much like the isotropic case, the low latent heat value causes planar solidification. Only slight instability is observable at t = 0.5s where there was no instability in the isotropic case. Figures 18-20 below show the case where K = 1.0.

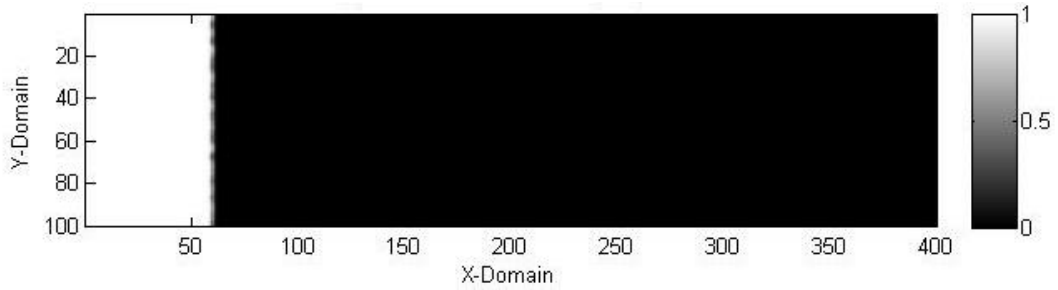

Fig. 18. Phase variable during anisotropic microstructure evolution when K = 1.0, step 500.

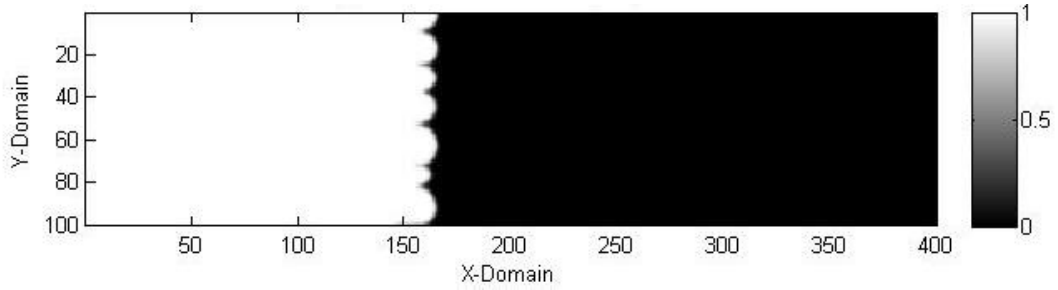

Fig. 19. Phase variable during anisotropic microstructure evolution when K = 1.0, step 1500.

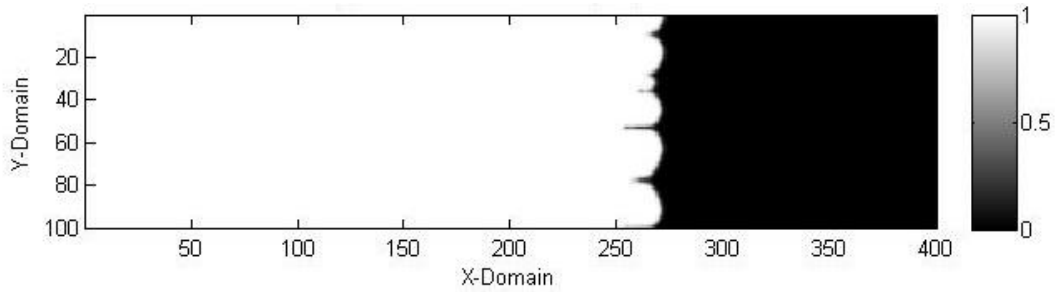

Fig. 20. Phase variable during anisotropic microstructure evolution when K = 1.0, step 2500.

For the case of K = 1.0, the solidification front begins to destabilize much sooner than the K = 0.8 case. As with the isotropic case, columnar roughness is observable at an early stage. Finally, the below figures (21-23) show the microstructure evolution for the case of K = 1.6.

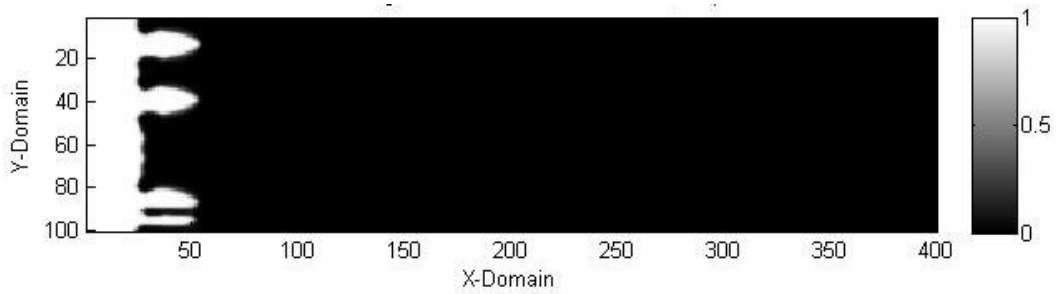

Fig. 21. Phase variable during anisotropic microstructure evolution when K = 1.6, step 500.

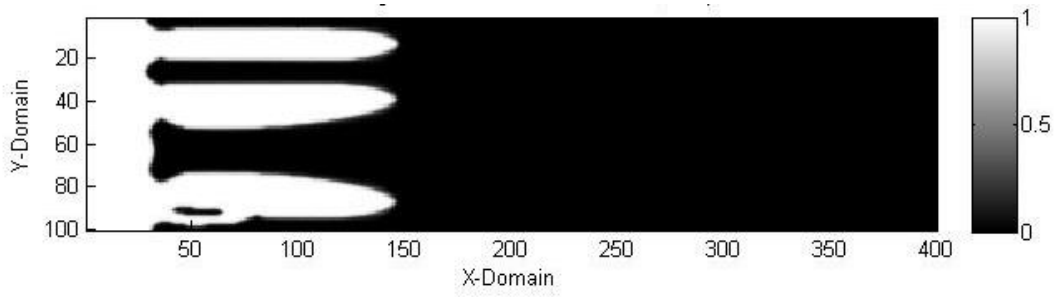

Fig. 22. Phase variable during anisotropic microstructure evolution when K = 1.6, step 1500.

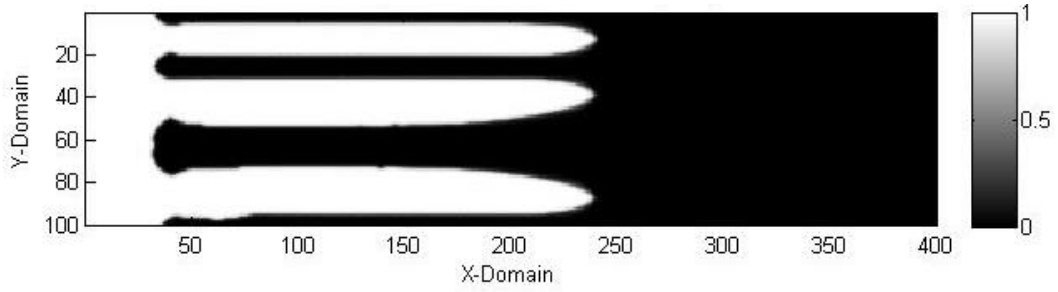

Fig. 23. Phase variable during anisotropic microstructure evolution when K = 1.6, step 2500.

As the latent heat increases, again we see a slowing of the growth and the formation of branches. Due to the four-mode anisotropy, the branches are nearly perfectly horizontal and have very little tendency to spread. This is to be expected for anisotropy in the *x*-direction and *y*-direction as is the case here.

4. NEW DISTRIBUTIONS

The developed MATLAB code will now be used to investigate various initial seed distributions and the effects of the latent heat on the growth of these systems. The box is now a square system of 200 pixels by 200 pixels. All other parameters remain unchanged. For these systems, as with every system in this work, the entire box is initially

undercooled (all values of the temperature field are zero at t = 0).The first distribution is a simple "four corners" distribution comprised of four 11x11 pixel seeds. The seeds are centered at the 50-pixel and 150-pixel mark in both *x*-domain and *y*-domain, so the seeds are symmetric about the center of the domain. Figures 24-27 below show the evolution of the system at step 0, step 500, step 1500, and step 2500. In these figures, $K = 1.4$.

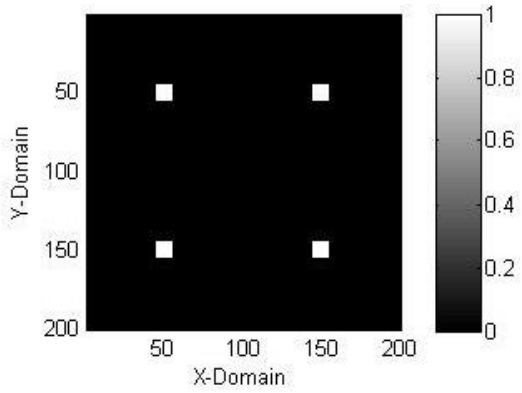

Fig. 24. Phase variable during isotropic microstructure evolution of "four corners" when $K = 1.4$, step 0.

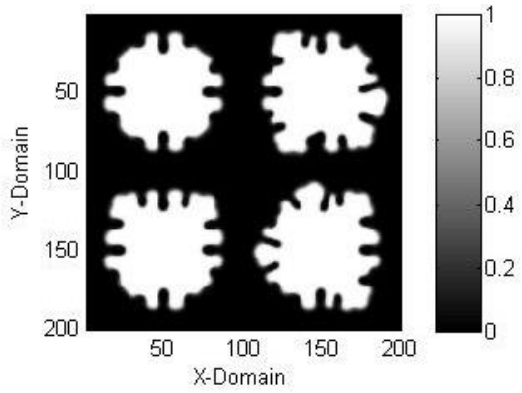

Fig. 25. Phase variable during isotropic microstructure evolution of "four corners" when $K = 1.4$, step 500.

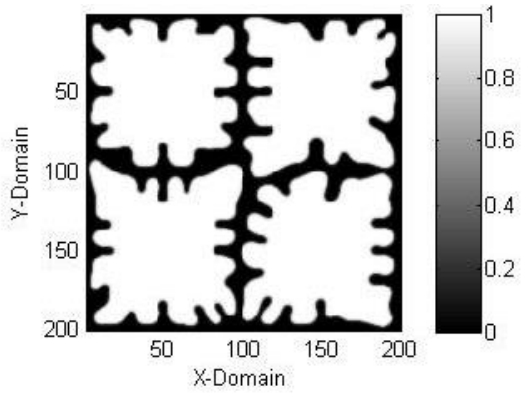

Fig. 26. Phase variable during isotropic microstructure evolution of "four corners" when *K* = 1.4, step 1500.

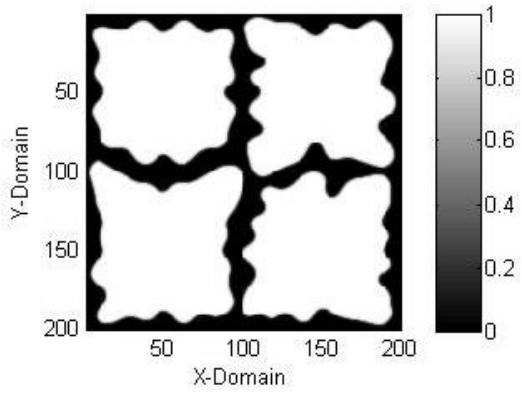

Fig. 27. Phase variable during isotropic microstructure evolution of "four corners" when *K* = 1.4, step 2500.

Each of the seeds grows outward and develops small branching tips at their edges. They continue to grow, and the tips retain their relative shortness, until most of the domain is solid and they no longer have room to continue expanding. The structures then start to fill out and lose their tip-like structures, becoming much more rounded or squared. They do this rather than merging with other structures, developing interfaces at each location where they come together. Figures 25-27 below show the same system when $K = 1.6$.

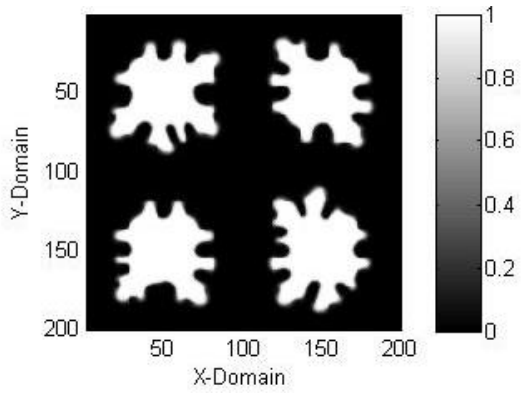

Fig. 28. Phase variable during isotropic microstructure evolution of "four corners" when *K* = 1.6, step 500.

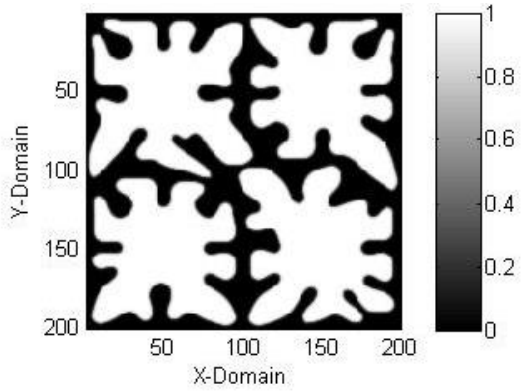

Fig. 29. Phase variable during isotropic microstructure evolution of "four corners" when *K* = 1.6, step 1500.

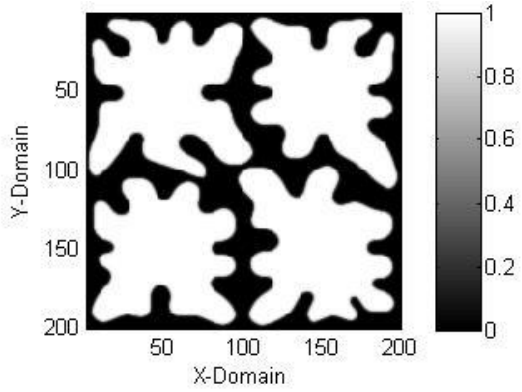

Fig. 30. Phase variable during isotropic microstructure evolution of "four corners" when *K* = 1.6, step 2500.

As expected, the structures become more pronounced with longer and more diverse tips compared to the case where K = 1.4. Growth is slower due to the higher latent heat, so the structures do not lose their notches at step 2500 as they did before. The main growth characteristics are the same, however; the seeds grow outward until they interface with each other and the edges of the box and then start to fill out.

A different seeding is examined in Figures 28-31 below. This "three points" seeding is comprised of three 11x11 pixel seeds in a triangular pattern. This case highlights the interfacing phenomenon of the growth. It is very clear from Figure 32 and Figure 33 that the interface where the three seeds come together is maintained while the growth continues into the open part of the domain, just as in the "four corners" distribution. The below figures (31-34) are for K = 1.4 and time steps 0, 500, 1500, and 2500.

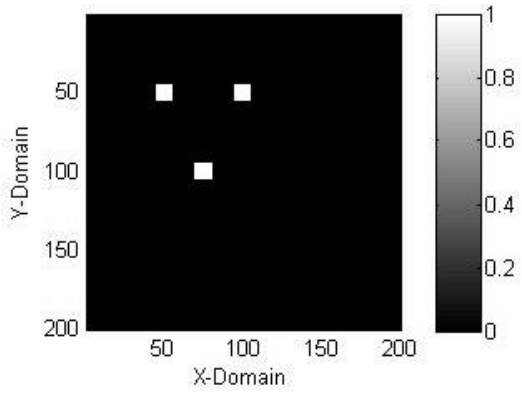

Fig. 31. Phase variable during isotropic microstructure evolution of "three points" when K = 1.4, step 0.

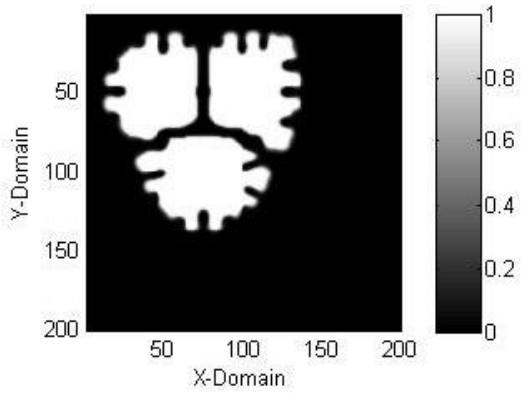

Fig. 32. Phase variable during isotropic microstructure evolution of "three points" when *K* = 1.4, step 500.

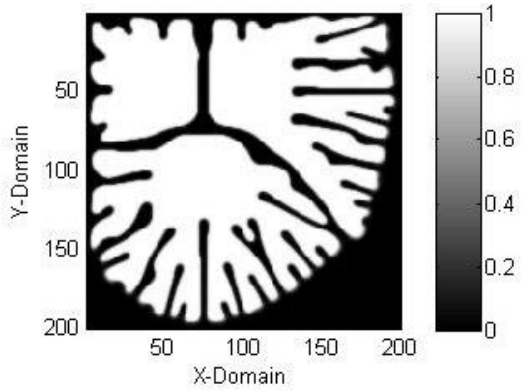

Fig. 33. Phase variable during isotropic microstructure evolution of "three points" when *K* = 1.4, step 1500.

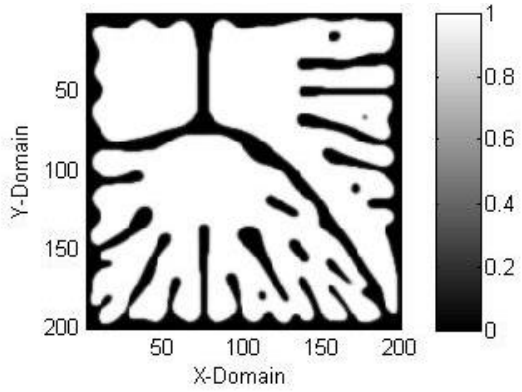

Fig. 34. Phase variable during isotropic microstructure evolution of "three points" when *K* = 1.4, step 2500.

Again, the seeds grow outward until they begin to interface with each other, at which time they spread away from each other to fill the remaining liquid region of the domain. There is very clear dendritic branching and these fingers stretch out into the other three corners from which the seeds did not originate. Comparing Figure 33 with Figure 34 again shows that the structures will begin to fill out and lose the deep grooves that make the fingers while keeping the interface between the seeds intact. This interface holds until past 7000 time steps, or t = 1.4 s.

The final seeding examined, the "stacked scatter", is shown in Figures 35-38 below. It consists of 25 pixels that are 6x6 symmetrically distributed through the top half of the box (thus, the upper part of the domain is stacked). This case is of interest because much more of the initial domain begins as solid, so effects are observed at earlier time steps than in the other cases. Furthermore, it provides a good opportunity to examine the effects of the random thermal noise. The figures below are for K = 1.4.

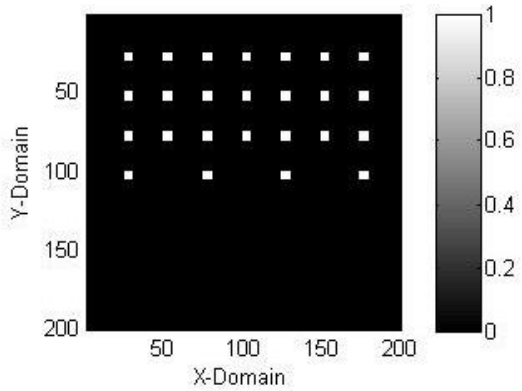

Fig. 35. Phase variable during isotropic microstructure evolution of "stacked scatter" when K = 1.4, step 0.

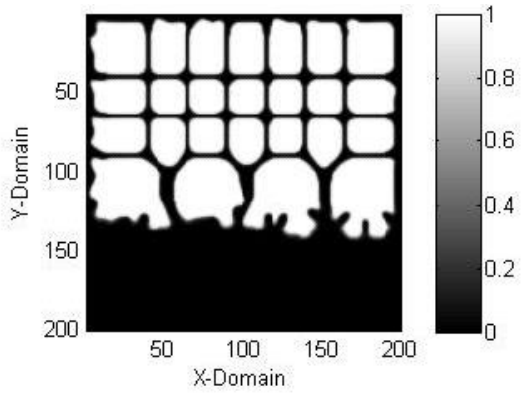

Fig. 36. Phase variable during isotropic microstructure evolution of "stacked scatter" when *K* = 1.4, step 500.

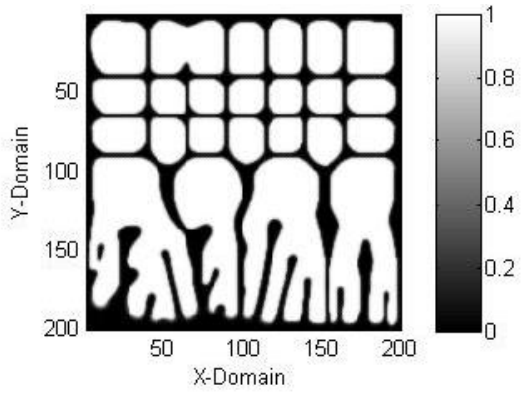

Fig. 37. Phase variable during isotropic microstructure evolution of "stacked scatter" when *K* = 1.4, step 1500.

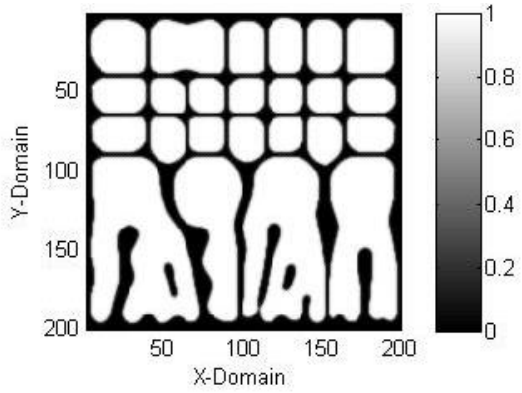

Fig. 38. Phase variable during isotropic microstructure evolution of "stacked scatter" when *K* = 1.4, step 2500.

Again, each of the seeds grows outward until it interfaces with other structures. In this case, with so many seeds, it forms a distinctive grid pattern. The structures tend not to merge with each other while there is still irregularity or roughness to their shape. These bumps (or the grooves seen in the previous cases) only encounter the thermal energy released by their own structures, rather than additionally seeing the energy released by the neighboring structures. Therefore, they are going to solidify first. Eventually the seeds will all be fairly round and smooth and have no choice but to begin merging, as can be seen in the top-left corner of both Figure 37 and Figure 38. The structures eventually merge in the previously shown systems, but it occurs much sooner in this case. While the structures in the top half are waiting to merge, the structures at the bottom finger out into the empty liquid region, as in the other cases.

As stated before, this distribution lends itself toward showcasing the effects of the random thermal noise. Figures 39-41 below are subsequent runs of the exact same simulation. All the parameters in the code are identical; the only difference between the figures is due to the random thermal noise term added to the $g(p)$ term.

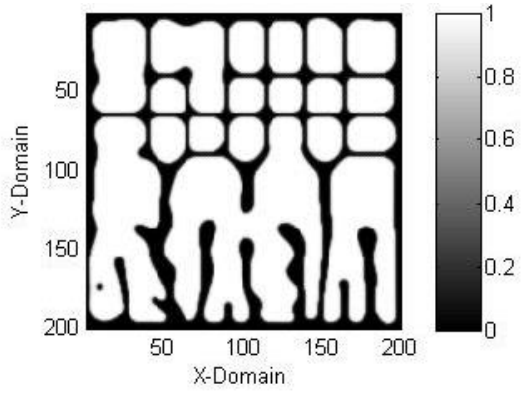

Fig. 39. Isotropic microstructure evolution of "stacked scatter" when K = 1.4, step 2000, first run.

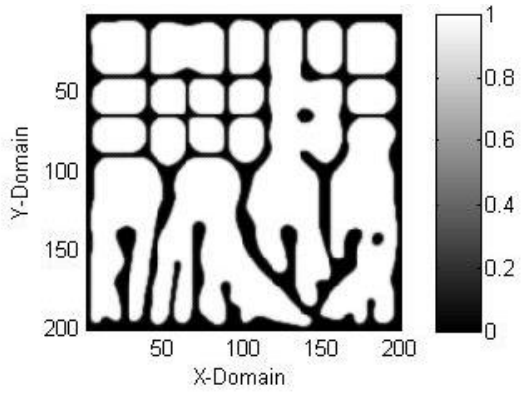

Fig. 40. Isotropic microstructure evolution of "stacked scatter" when *K* = 1.4, step 2000, second run.

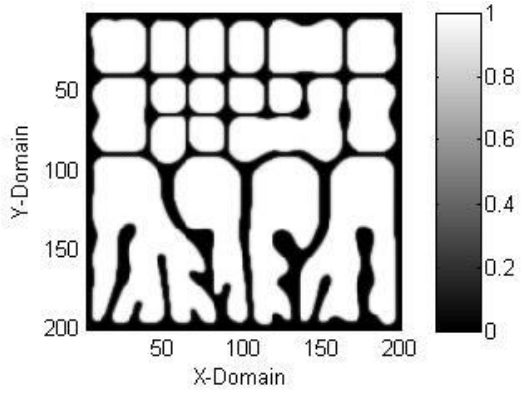

Fig. 41. Isotropic microstructure evolution of "stacked scatter" when *K* = 1.4, step 2000, third run.

In each figure, the growth patterns are the same but the specific structures are different. In Figure 39, many of the structures on the far left side merge, and all branches are allowed to extend fully to the bottom of the domain. However, in Figure 40, the far left structures do not merge and there is competition between branches that cuts off one of the structures from reaching the bottom. In Figure 41, three of the structures just above the branching structures merge, where they didn't in the previous two cases. All of this showcases the effects of the random thermal noise addition.

5. CASTING DISTRIBUTIONS

The above novel seeding distributions were of interest to investigate the growth behavior of the system modeled with the MATLAB code. The expansion, interfacing, filling out, and merging phenomena are exhibited nicely. However, the main interest and application of the code is for simulation of casting processes. The above systems do not represent well a casting scenario because the growth is homogeneous and the seeds originate in the center of the domain. During the casting process, the nucleation will occur heterogeneously and on the edge of the domain. Therefore, several systems are examined below to see how this difference affects the growth behavior. Latent heat differences were investigated above, and will not be addressed again here. A value of K = 1.4 was chosen because it exhibits the behaviors of interest while not taking as long to simulate as a value of K = 1.6 would.

The first system is a simple system in which the edges of the domain each have a continuous wall of solid that is ten pixels wide. Figures 42-45 below show the evolution of the system at time steps 0, 500, 1500, and 2500 when K = 1.4.

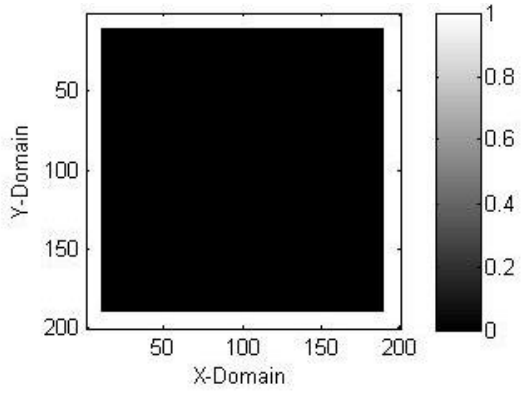

Fig. 42. Isotropic microstructure evolution of "all around" casting distribution when K = 1.4, step 0.

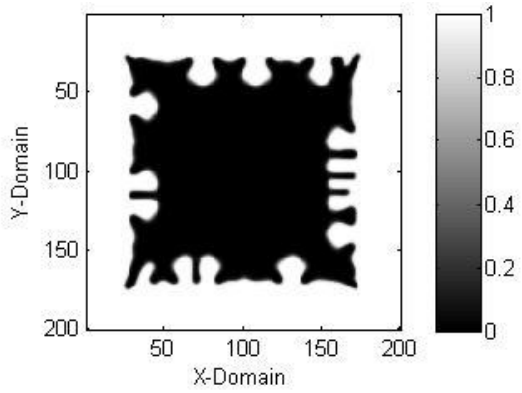

Fig. 43. Isotropic microstructure evolution of "all around" casting distribution when *K* = 1.4, step 500.

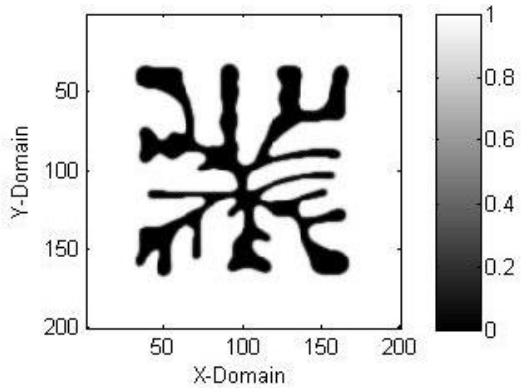

Fig. 44. Isotropic microstructure evolution of "all around" casting distribution when *K* = 1.4, step 1500.

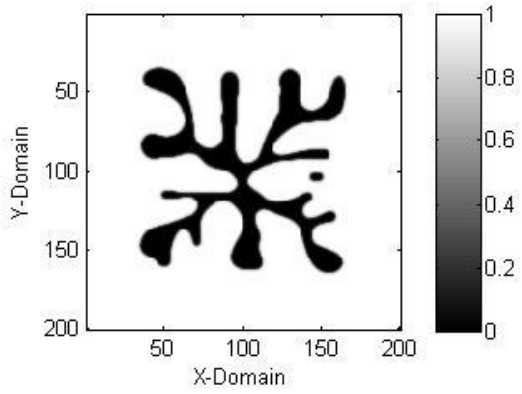

Fig. 45. Isotropic microstructure evolution of "all around" casting distribution when *K* = 1.4, step 2500.

With the perfect heterogeneous nucleation along the edges of the domain, the system is similar to that of the Kobayashi systems and the growth is similar. There is slight fingering or dendrite formation from the wall of solid and these structures propagate through the system. Then, as expected from the novel distributions in the previous section, they meet each other, interface, begin to lose their finger-like structure, and fill out. Very little merging is seen at 2500 steps.

The second system is much like the first except that the initial seed is not a solid wall but rather many discrete seeds around the edge of the domain. Figures 46-49 below show the evolution of the system at time steps 0, 500, 1500, and 2500 when $K = 1.4$.

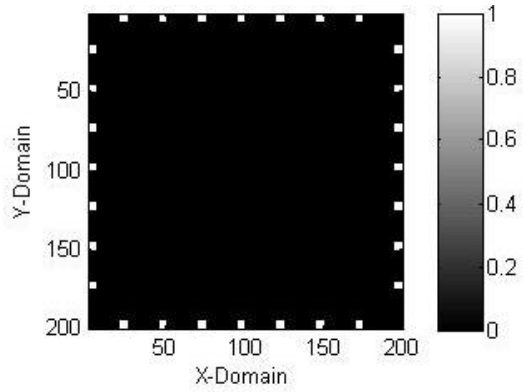

Fig. 46. Isotropic microstructure evolution of "scatter" casting distribution when $K = 1.4$, step 0.

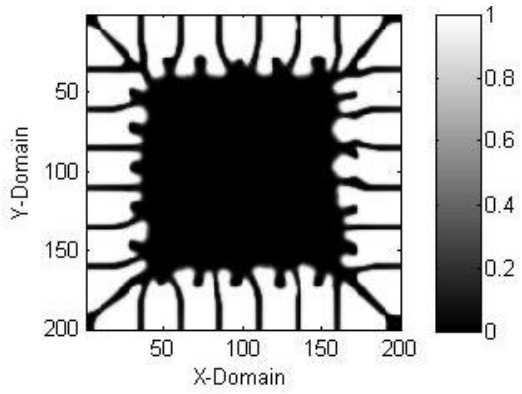

Fig. 47. Isotropic microstructure evolution of "scatter" casting distribution when *K* = 1.4, step 500.

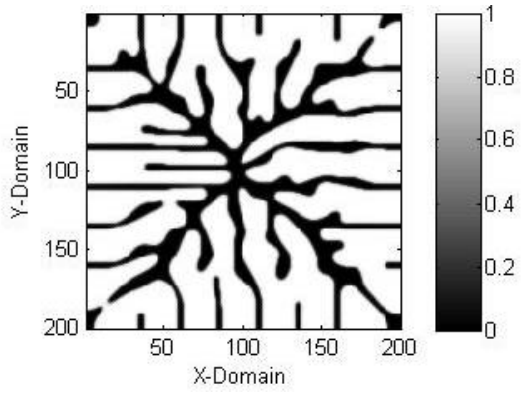

Fig. 48. Isotropic microstructure evolution of "scatter" casting distribution when *K* = 1.4, step 1500.

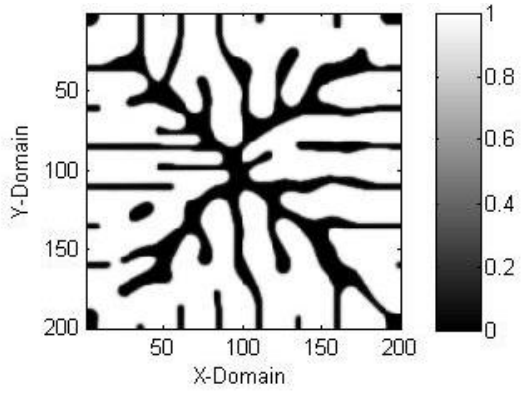

Fig. 49. Isotropic microstructure evolution of "scatter" casting distribution when *K* = 1.4, step 2500.

The growth of each seed is quite columnar for the first 500 time steps, as opposed to the "all around" casting system where a few fingers initiate and propagate from the solid wall. The columns then become dendritic fingers as the branches closer to the corners are cut off by their counterparts on the adjacent wall. This leads to an X-shaped interface, with the structures in the center of each wall typically being the longest. Afterward there occurs the expected filling out and some merging begins in the corners where the tips of the structures have halted.

The behavior of the "scatter" system is very representative of an actual casting scenario. Theoretically, a casting microstructure consists of three zones: the chill region, the columnar region, and the equiaxed region; this is shown in Figure 50 below [1]:

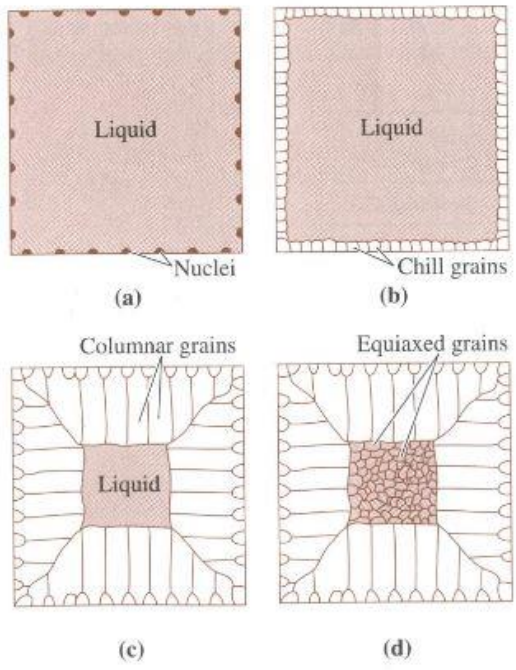

Fig. 50. Theoretical casting microstructure, including chill region, columnar region, and equiaxed region.

Figure 50(a) shows the initial heterogeneous nucleation that takes place along the mold wall, similar to the initial seeding in Figure 46, except that the real nuclei are hemispherical rather than square. Realistically, homogenous nucleation occurs spherically due to its energetically favorable low surface-area-to-volume ratio. If there is a strong interaction with the edge of the casting surface, the round nucleus will spread and become wider and shallower. On the other hand, if the interaction is not strong it will remain more globular. Regardless, the approximation as a square is sufficient. This heterogeneous nucleation occurs because a full spherical nucleus is not required; rather, a hemispherical nucleus is formed due to the contact with the wall, which requires less energy. Figures 50(b) and 50(c) correspond to Figure 47, showing the chill region and columnar region. The chill region consists of randomly oriented grains that are the first to solidify from the nuclei [1]. However, as this model does not (yet) track the crystallographic orientation of the solid, this chill region gets lost in the columnar region. As thermal energy is conducted back through grains and into the wall of the mold, the grains begin to grow in the direction of this large energy gradient perpendicular to the wall. This is the reason for the columnar region. Finally, the equiaxed region in Figure 50(d) is formed by spontaneous nucleation that frequently occurs either because of inoculating agents or small grains from the chill region being transported by convection currents during freezing [1]. The MATLAB code in this work does not allow for spontaneous nucleation but rather only growth from the initial seeding, so the equiaxed region does not occur. Instead, the X-shaped interface described above occurs as the dendrites that are not cut off continue to grow. This interface can even be seen in Figure 50(c) and Figure 50(d), until it reaches the square equiaxed region. A real system

showing columnar and equiaxed growth in a casting system is shown in Figure 51 below, from the experimental work on Al-Fe performed by Ribeiro et al. [15].

Fig. 51. Columnar and equiaxed growth in an Al-Fe alloy shown experimentally by Ribeiro et al.

The solidification is singularly directional rather than from four sides as in the case of this work, but there is clear columnar growth from the bottom and a clear equiaxed region near the top. This experimentally supports the theoretical principles discussed above.

6. CONCLUSION

Above, the Kobayashi model was studied and described, then developed into a MATLAB code. The code was successfully able to not only replicate the systems

described by Kobayashi, but also to successfully describe casting scenarios supported by experiment. Theoretically, increasing the latent heat parameter should have the effect of slowing down the growth in order for the thermal energy removal process to match such heating. This was found to be the case in the simulations.

For the novel seeding distributions, a single apparent growth pattern was followed in each system. The seeds would grow outward until they got near to other structures, after which they would form an interface between the structures and be disinclined to merge. The parts of the solid not at one of these interfaces would fill out and begin to lose dendritic shape because they were subject to less latent heating, being away from the strong interface. After some time, the structures would eventually overcome this interface and merge across it. As mentioned in the discussion of the "scatter" system, this merging occurs because the MATLAB code does not track crystallographic orientation. All solid is treated characteristically as the same. If grain boundaries and orientations were explicitly tracked, the misorientation across these interfaces would disallow such merging and the gap would be filled in by subsequent solidification at a third orientation.

Finally, the MATLAB code was employed to simulate a casting scenario, and the growth behavior seen was typical of that solidification technique. The chill, columnar, and equiaxed regions predicted by theory were indeed able to be explained with the model, although with some extra justification. The columnar region was very obviously present, but the chill region was lost in the columnar region due to the mentioned lack of grain orientation tracking. Also, the equiaxed region (which does not occur in every single casting scenario), was impossible to produce because the code does not allow for

spontaneous nucleation after the initial conditions are established. However, future work could further develop the code and completely exhibit these phenomena.

In fact, this next step in the investigation has already been taking place. Work has been done to study the model of Warren et al. [8] that would track crystallographic orientation of pure polycrystalline materials. The free energy functional would be modified to include orientation, developing a three-field model of phase, orientation, and temperature. A similar process to that described in Section 2 would be followed: initial conditions would be established, boundary conditions would be set up, and the three fields would be incrementally evolved over many time steps. The primary addition would be the orientation field and the calculation of the magnitude of the gradient of theta. Of course, there are many nuances and the extension of the model to include grain orientation is not as straightforward as that. That work is being performed by a Ph.D. student in the Spearot group, and at the writing of this paper is close to completion.

References

[1] D.R. Askeland, P.P. Fulay, Essentials of Materials Science and Engineering, second ed., Toronto, Ontario, 2009.

[2] OICA, "2013 Production Statistics", http://www.oica.net/category/production-statistics/2013-statistics/ (last accessed 4/7/15).

[3] N. Moelans, B. Blanpain, P. Wollants, An introduction to phase-field modeling of microstructure evolution, Comp. Coupling Phase Diag. Thermochem. 32 (2008) 268-294.

[4] L.Q. Chen, Phase-field models for microstructure evolution, Annu. Rev. Mater. Res. 32 (2002) 113-140.

[5] K. Thornton, J. Agren, P.W. Voorhees, Modelling the evolution of phase boundaries in solids at the meso- and nano-scales, Acta Mater. 51 (2003) 5675-5710.

[6] R. Kobayashi, Modeling and numerical simulations of dendritic crystal growth, Physica D 63 (1993) 410-423.

[7] W.J. Boettinger, J.A. Warren, C. Beckermann, A. Karma, Phase-field simulation of solidification, Annu. Rev. Mater. Res. 32 (2002) 163-194.

[8] J.A. Warren, R. Kobayashi, A.E. Lobkovsky, W.C. Carter, Extending phase field models of solidification to polycrystalline materials, Acta Mater. 51 (2003) 6035-6058.

[9] B.P. Athreya, N. Goldenfeld, J.A. Dantzig, M. Greenwood, N. Provatas, Adaptive mesh computation of polycrystalline pattern formation using a renormalization-group reduction of the phase-field crystal model, Phys. Rev. E 76 (2007) 056706.

[10] L. Granasy, T. Pusztai, J.A. Warren, Modelling polycrystalline solidification using phase field theory, J. Phys.: Condens. Matter 16 (2004) R1205-R1235.

[11] J.H. Mathews, K.D. Fink, Numerical Methods Using MATLAB, fourth ed., New Jersey, USA, 2004.

[12] D. Kuzmin, Power Point Slides, http://www.mathematik.uni-dortmund.de/~kuzmin/cfdintro/lecture4.pdf (last accessed 4/7/15).

[13] R.J. Kirkpatrick, Crystal growth from the melt: a review, Amer. Mineral. 60 (1975) 798-814.

[14] A.A. Wheeler, B.T. Murray, R.J. Schaefer, Computation of dendrites using a phase field model, Physica D 66 (1993) 243-262.

[15] P.L. Ribeiro, B.L. Silva, W.S. Silva, J.E. Spinelli, Effects of cellular growth on fatigue life of directionally solidified hypoeutectic Al-Fe alloys, Mater. Res. 17(3) (2014) 767-774.